Varied proton conductivity and photoreduction CO_2 performance in isostructural heterometallic clusters based metal−organic frameworks

Hai-Ning Wang,[a] Hong-Xu Sun,[a] Yao-Mei Fu,[b] Xing Meng,*[a] Yan-Hong Zou,[a] Yu-Ou He,[a] Rui-Gang Yang[a]

[a]School of Chemistry and Chemical Engineering, Shandong University of Technology, Zibo 255049, People's Republic of China.

E-mail: mengxing837@foxmail.com

[b]Shandong Engineering Research Center of Green and High-value Marine Fine Chemical; Weifang University of Science and Technology, Shouguang 262700, People's Republic of China.

Table S1 The Fe and M (M=Co and Ni) mole ratio in **MOF-Fe$_2$Co** and **MOF-Fe$_2$Ni** crystals by ICP analysis.

Sample	Concentration of Fe (μg/mL)	Concentration of M (μg/mL)	Fe:M
MOF-Fe$_2$Co	8.544	4.480	2.009
MOF-Fe$_2$Ni	9.273	4.892	1.997

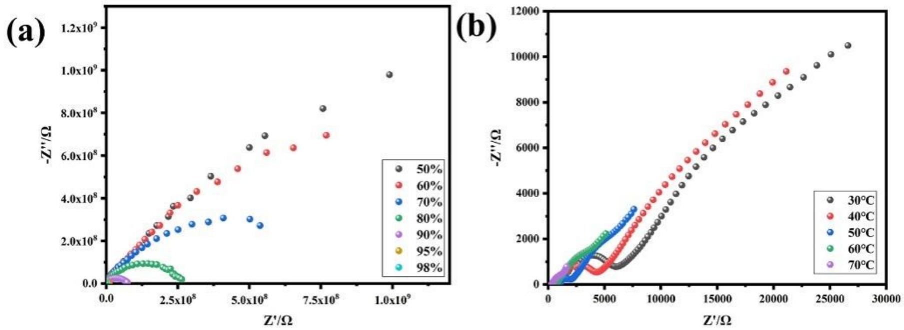

Fig. S1 Impedance spectrum of **MOF-Fe$_3$** at 30°C with different RHs (a) and 98 % RH under different temperatures (b).

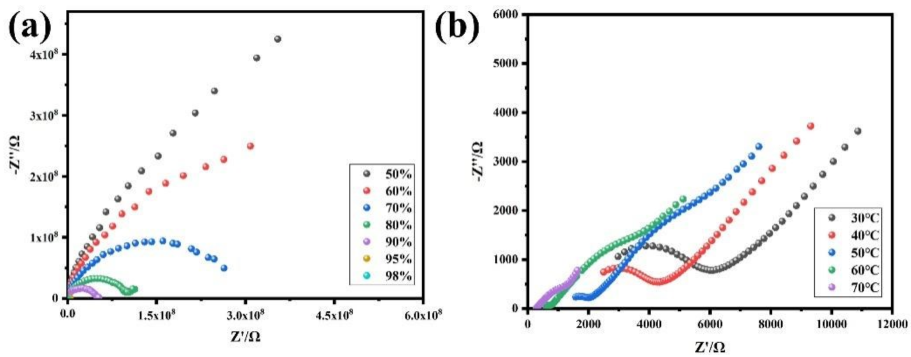

Fig. S2 Impedance spectrum of **MOF-Fe_2Co** at 30 °C with different RHs (a) and 98 % RH under different temperatures (b).

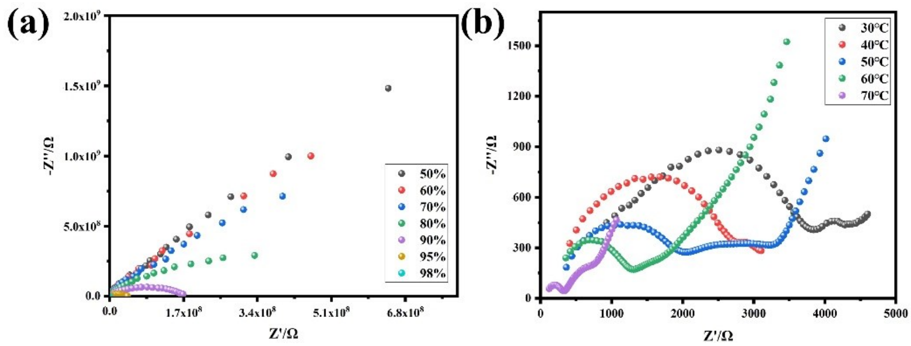

Fig. S3 Impedance spectrum of **MOF-Fe_2Ni** at 30°C with different RHs (a) and 98 % RH under different temperatures (b).

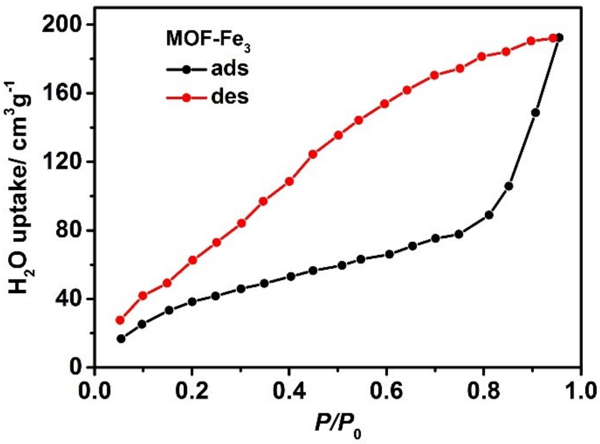

Fig. S4 Water vapor adsorption and desorption isotherms of **MOF-Fe_3**.

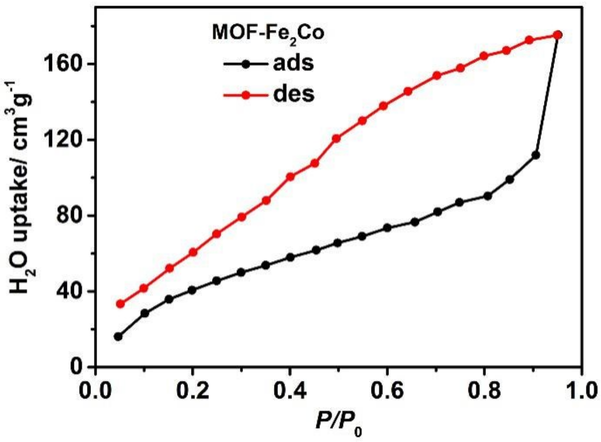

Fig. S5 Water vapor adsorption and desorption isotherms of **MOF-Fe$_2$Co**.

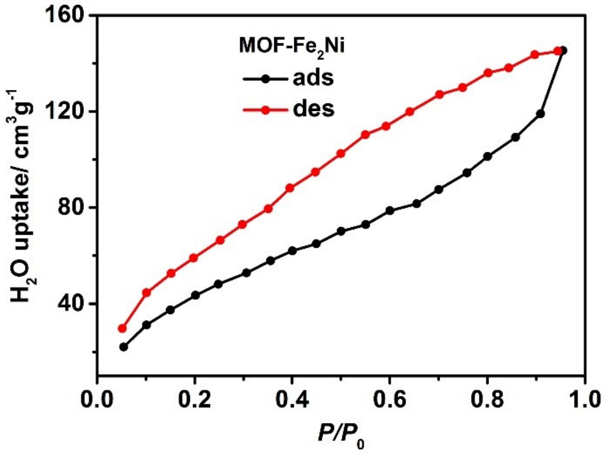

Fig. S6 Water vapor adsorption and desorption isotherms of **MOF-Fe$_2$Ni**.

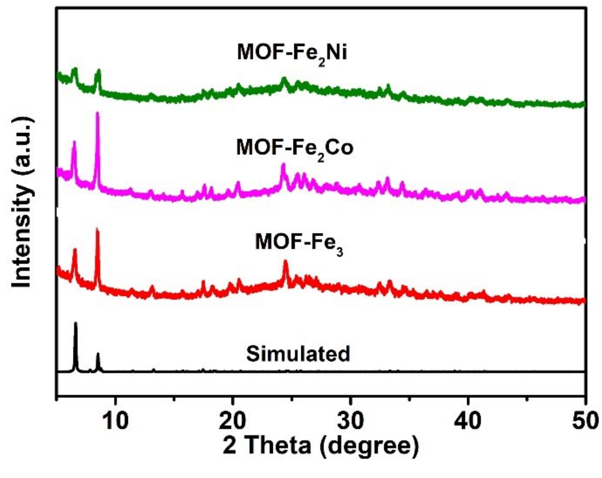

Fig. S7 PXRD patterns of **MOF-Fe$_2$M** after proton conductive measurements.

Table S2 Proton conductive MOFs and their proton conductivity.

Materials	Proton conductivity (S cm^{-1})	Condition	Refs.
Im-Fe-MOF	1.21×10^{-2} S·cm^{-1}	60˚C, 98% RH	1

Im@MOF-808	3.45 × 10^{-2} S·cm^{-1}	60˚C, 99% RH	2
KAUST-7	2.0 × 10^{-2} S·cm^{-1}	90˚C, 95% RH	3
Co-fdc	4.85 × 10^{-3} S·cm^{-1}	80˚C, 98% RH	4
Im-Cu@(NENU-3a)	3.16 × 10^{-4} S·cm^{-1}	70˚C, 90% RH	5
Ni-BDP	2.22 × 10^{-3} S·cm^{-1}	80˚C, 97% RH	6
$[Ni_8(OH)_4(H_2O)_2(BDPCOOH)_6]$	2.22 × 10^{-3} S·cm^{-1}	80˚C, 97% RH	6
MOF-801	1.88 × 10^{-3} S·cm^{-1}	25˚C, 98% RH	7
Cu^I-MOF·pz·3H_2SO_4	3.0 × 10^{-3} S·cm^{-1}	70˚C, 95% RH	8
$\{Na[Cd(MIDC)]\}_n$	1.04 × 10^{-3} S·cm^{-1}	100˚C, 98% RH	9
$(H[Ln(H_2O)_4]_2[MnV_{13}O_{38}]\cdot 9NMP\cdot 17H_2O$ (Ln=Ce and La)	4.68/3.46×10^{-3} S·cm^{-1}	61˚C, 97% RH	10
MFM-510	2.1 × 10^{-5} S·cm^{-1}	25 ˚C, 99% RH	11
Ho-MOF ($[Ho(SIP)(H_2O)_5]\cdot 3H_2O$	8.2×10^{-4} S·cm^{-1}	70 ˚C, 99% RH	12
TMOF-2	1.23 × 10^{-4} S·cm^{-1}	90 ˚C, 98% RH	13
MIT-25	5.1 × 10^{-4} S·cm^{-1}	75 ˚C, 95% RH	14
$[CH_3NH_3]2[H_3O]Ag_5Sn_4Se_{12}\cdot C_2H_5OH$	2.62 ×10^{-4} S·cm^{-1}	60 ˚C, 99% RH	15
ZZU-2	4.63×10^{-4} S·cm^{-1}	98˚C,100% RH	16

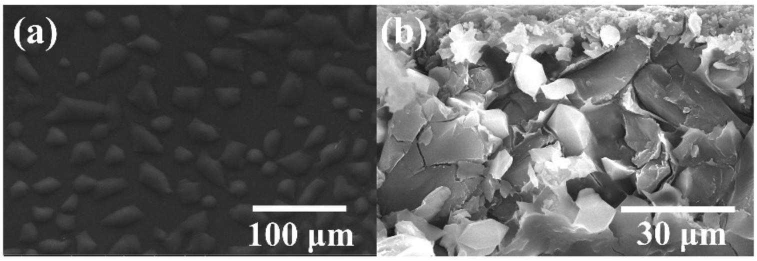

Fig. S8 SEM images of surface (left) and cross section (right) of **MOF-Fe_3@PP-20** composite membrane.

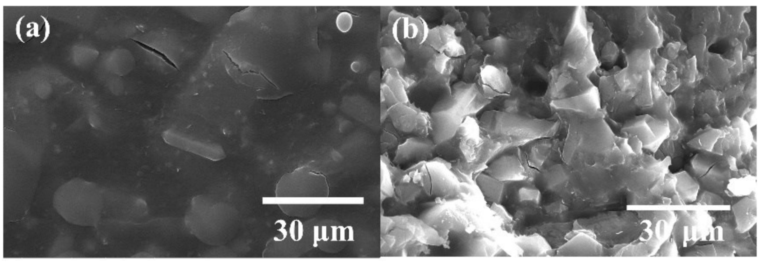

Fig. S9 SEM images of surface (left) and cross section (right) of **MOF-Fe_3@PP-40** composite membrane.

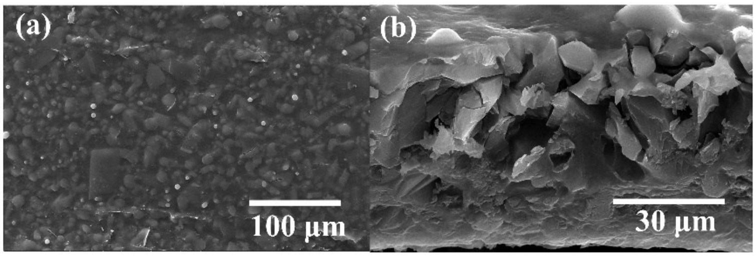

Fig. S10 SEM images of surface (left) and cross section (right) of **MOF-Fe_3@PP-60** composite membrane.

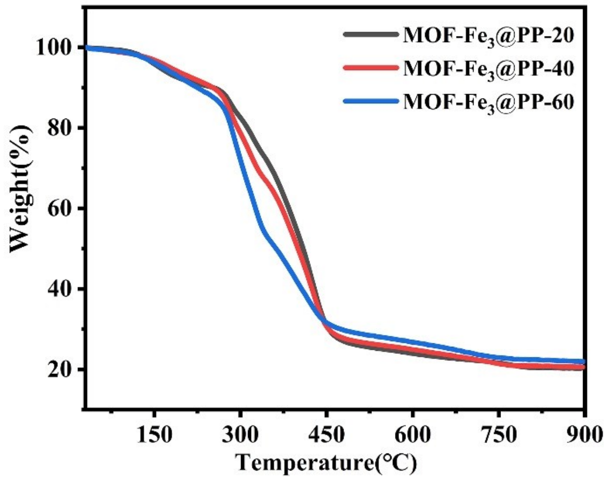

Fig. S11 The TG plots of three membranes.

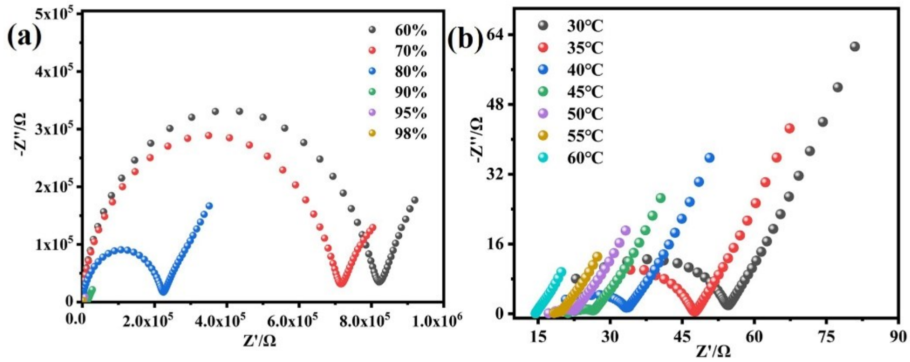

Fig. S12 Impedance spectra of **MOF-Fe_3@PP-20** composite membrane at 30 °C with different RHs (a) and 98% RH under different temperatures (b).

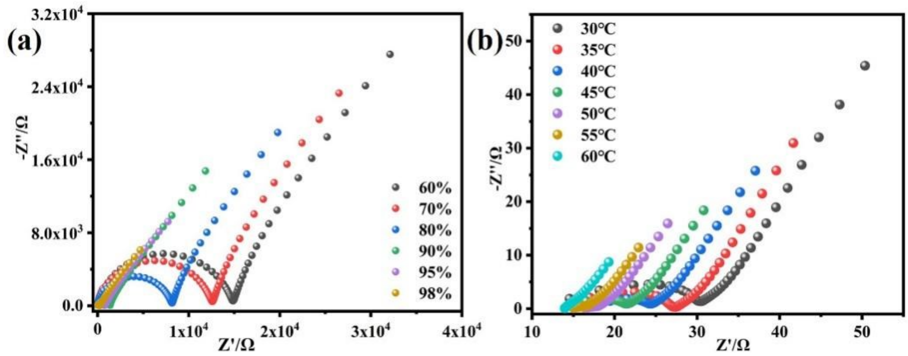

Fig. S13 Impedance spectra of **MOF-Fe_3@PP-40** composite membrane at 30 °C with different RHs (a) and 98% RH under different temperatures (b).

Table S3 The proton conductivity of three membranes under different temperatures with 98% RHs.

Temperature (°C)	Conductivity of **MOF-Fe_3@PP-20** (S cm^{-1})	Conductivity of **MOF-Fe_3@PP-40** (S cm^{-1})	Conductivity of **MOF-Fe_3@PP-60** (S cm^{-1})
30°C	6.01×10^{-4}	8.87×10^{-4}	1.76×10^{-3}
35°C	7.10×10^{-4}	1.14×10^{-3}	2.18×10^{-3}
40°C	1.09×10^{-3}	1.37×10^{-3}	2.50×10^{-3}
45°C	1.45×10^{-3}	1.85×10^{-3}	3.02×10^{-3}
50°C	1.99×10^{-3}	2.16×10^{-3}	3.53×10^{-3}
55°C	2.15×10^{-3}	3.00×10^{-3}	3.95×10^{-3}
60°C	2.47×10^{-3}	3.63×10^{-3}	5.46×10^{-3}

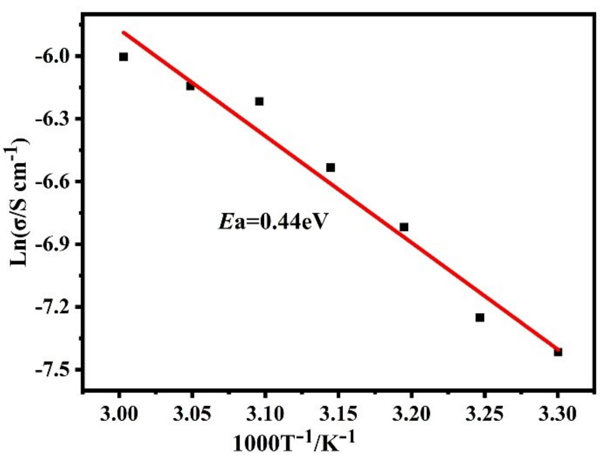

Fig. S14 Arrhenius plot of the proton conductivities of **MOF-Fe$_3$@PP-20** composite membrane.

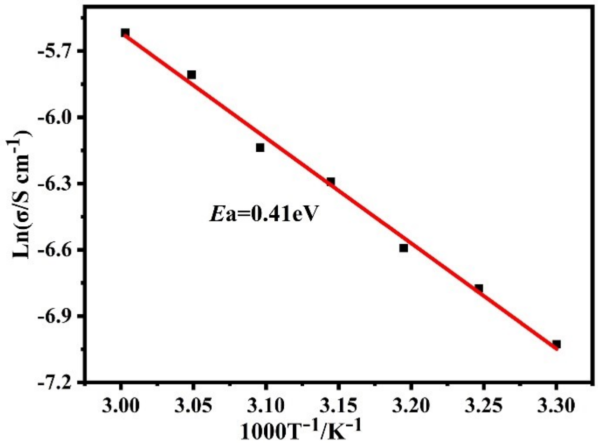

Fig. S15 Arrhenius plot of the proton conductivities of **MOF-Fe$_3$@PP-40** composite membrane.

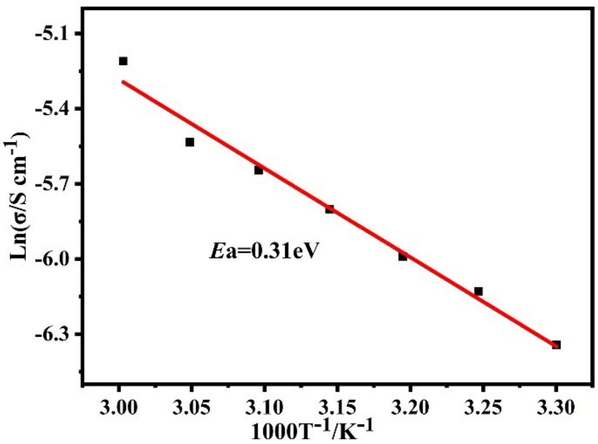

Fig. S16 Arrhenius plot of the proton conductivities of **MOF-Fe$_3$@PP-60** composite membrane.

Table S4 The proton conductive MOFs and their proton conductivity.

Materials	**Proton conductivity (S cm^{-1})**	**Condition**	**Refs.**
MOF-801@PP-X	1.88×10^{-3} S·cm^{-1}	98% RH, 25°C	7
JUC-200@PVA-X	1.25×10^{-3} S·cm^{-1}	100% RH, 25°C	17
MOF-808@PVDF-55	1.56×10^{-4} S·cm^{-1}	100% RH, 65°C	18
SPEE/S-UiO-66@GO-10	1.657×10^{-3} S·cm^{-1}	40% RH, 100°C	19
HPW@MIL-101/SPEEK	6.51×10^{-3} S·cm^{-1}	40% RH, 60°C	20
CS/CMMIM@MIL-53(Fe)-75%	2.1×10^{-3} S·cm^{-1}	70% RH, 15°C	21
PMoV$_2$@MIL-101-11.2	6.31×10^{-3} S·cm^{-1}	98% RH, 80°C	22
MOF-808-OX@PVA-3	2.1×10^{-5} S·cm^{-1}	98% RH, 30°C	23

Nafion/SmH_2SP-5	2.61×10^{-2} S·cm^{-1}	100% RH, 90°C	24
VMT-CNFs	4.3×10^{-2} S·cm^{-1}	100% RH, 100°C	25
Cr/sBDC-Gel-0.4 M	7.84×10^{-3} S·cm^{-1}	100% RH, 80°C	26
TEPA@ZIF-8-H_2CO_3	5.38×10^{-3} S·cm^{-1}	99% RH, 60°C	27

Table. S5 The formation rates of different products under different irradiation times and the selectivity of CO.

Samples	Irradiation time	The formation rate of CO (μmol·g^{-1}·h^{-1})	The formation rate of CH_4 (μmol·g^{-1}·h^{-1})	The formation rate of H_2 (μmol·g^{-1}·h^{-1})	The selectivity of CO
MOF-Fe_3	4.0h	6.08	0	0.27	95.7%
MOF-Fe_2Co	4.0h	16.29	0	0.637	96.2%
MOF-Fe_2Ni	4.0h	18.41	0	0.31	98.4%
MOF-Fe_3	8.0h	4.53	0	0.18	96.1%
MOF-Fe_2Co	8.0h	13.19	0	0.095	99.3%
MOF-Fe_2Ni	8.0h	15.81	0	0.63	96.2%

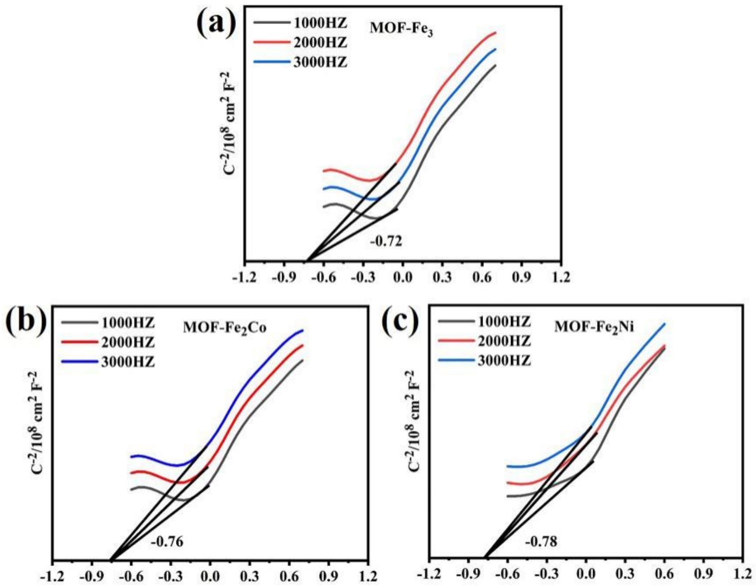

Fig. S17 Mott-Schottky plots of **MOF-Fe_3** (a), **MOF-Fe_2Co** (b) and **MOF-Fe_2Ni** (c).

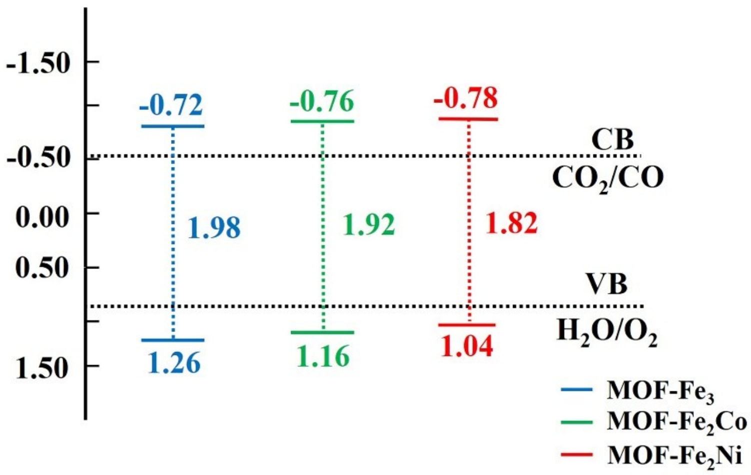

Fig. S18 Energy level plots of **MOF-Fe$_2$M**.

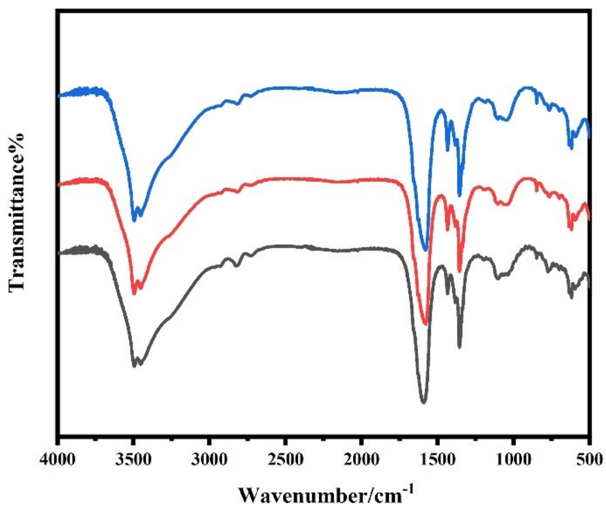

Fig. S19 FTIR spectra of **MOF-Fe$_3$** (black), after proton conductivity testing (red) and photocatalysis testing (blue).

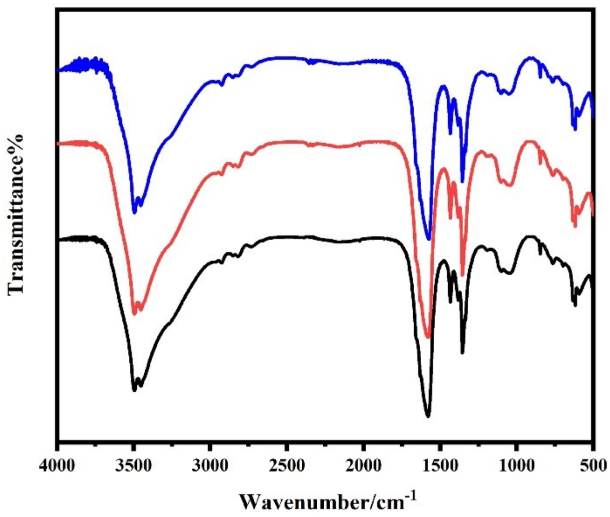

Fig. S20 FTIR spectra of **MOF-Fe_2Co** (black), after proton conductivity testing (red) and photocatalysis testing (blue).

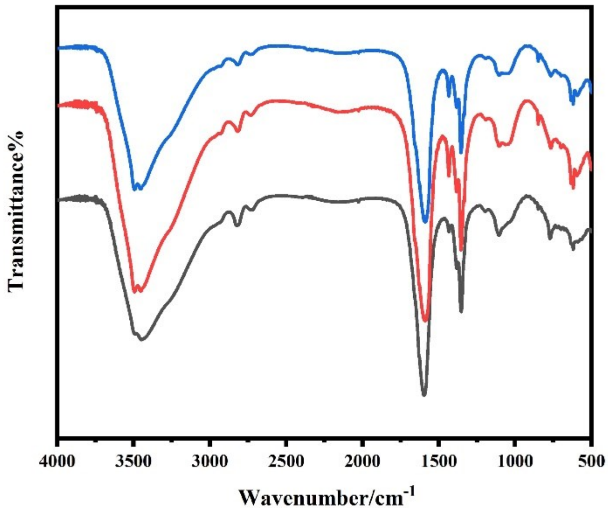

Fig. S21 FTIR spectra of **MOF-Fe_2Ni** (black), after proton conductivity testing (red) and photocatalysis testing (blue).

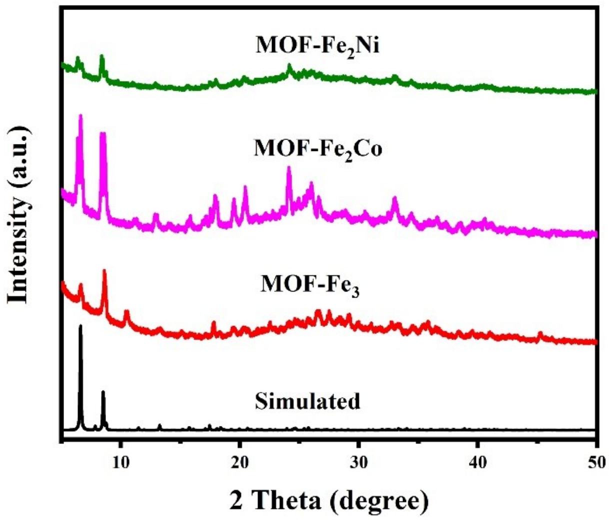

Fig. S22 PXRD patterns of **MOF-Fe_2M** after photocatalysis testing.

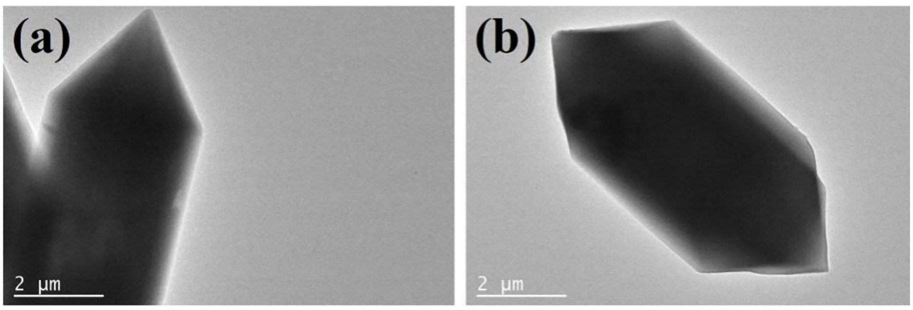

Fig. S23 The TEM images of **MOF-Fe_2Ni** before (a) and after (b) CO_2 photoreduction.

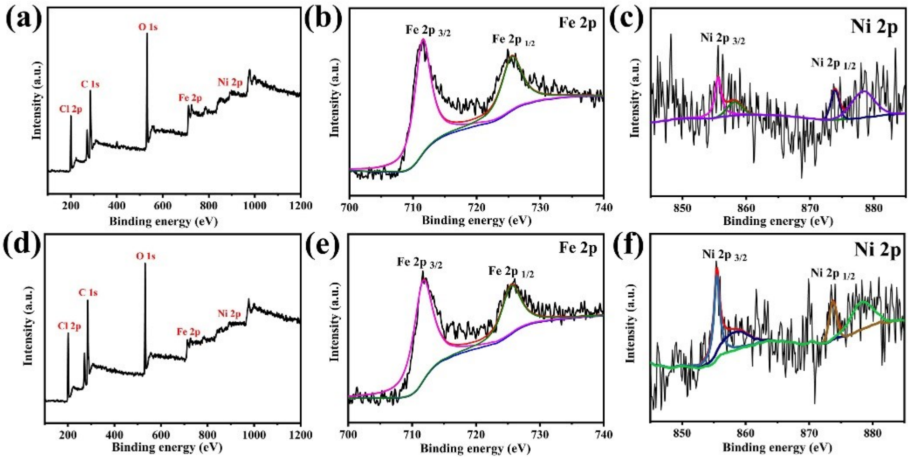

Fig. S24 XPS spectra of **MOF-Fe$_2$Ni** before (a) and after (b) CO_2 photoreduction.

Table S6 The photocatalytic performances of MOFs.

Material	Products and yields	Reaction pattern	Photosensitizer/Sacrifice agent	
PCN-221(Fe0.2)	CO 0.52 μmol $g^{-1}h^{-1}$	Solid-liquid	ethyl acetate/H_2O	28
$Cu_3(BTC)_2$	CO 11.48 μmol $g^{-1}h^{-1}$	Solid-liquid	CO_2/H_2O vapor	29
HKUST-1	CO 4.537 μmol g^{-1} h^{-1}	Solid-gas	erephthalic acid	29
Ag⊂Re$_3$-MOF-16 nm	CO _	Solid-liquid	MeCN/TEA (20:1)	30
Fe-MIL-101-NH_2	CO 4.7 μmol $g^{-1}h^{-1}$ H_2 2.1 μmol $g^{-1}h^{-1}$	Solid-liquid	MeCN/H_2O/ TEOA (3:2:1)	31
AD-MOF-2	HCOOH 443.2 μmol g^{-1} h^{-1}	Solid-liquid	aqueous solution	32
MOF-253-Ru(dcbpy)$_2$	CO 3.3 μmol $g^{-1}h^{-1}$ HCOOH 26.7 μmol$g^{-1}h^{-1}$	Solid-liquid	MeCN (2 mL)	33
Zr-MOF-525	CO 1.52 μmol $g^{-1}h^{-1}$ CH_4 0.5 μmol $g^{-1}h^{-1}$	Solid-liquid	H_2O	34
MAF-7	formic acid 1.52 mmol $g^{-1}h^{-1}$	Solid-liquid	phosphate uffer (100 mM, pH=7), TEOA(15w/v%)	35
Co-UiO-67	CO 329 μmol $g^{-1}h^{-1}$ H_2 709 μmol $g^{-1}h^{-1}$	Solid-liquid	MeCN/H_2O/TEOA= 4:1:1	36
NH_2-MIL-125	CH_4 0.69 μmol $g^{-1}h^{-1}$	Solid-liquid	H_2O	37
PCN-224(Cu)	CO 3.72 μmol g^{-1} h^{-1}	Solid-liquid	_	38
MIL-101-Cr	CO 8.3 μmol g^{-1} h^{-1} CH_4 1.7 μmol $g^{-1}h^{-1}$	Solid-liquid	H_2O and TEOA	39
NNU-31-Zn	HCOOH 1.7 μmol $g^{-1}h^{-1}$	Solid-liquid	H_2O	40
NH_2-MIL-125(Ti)	CO 0.76 μmol g^{-1} h^{-1}	Solid-liquid	Acetonitrile (3mL) triethanolamine (1	41

			mL)	
ZIF-8	CO 0.68 μmol g^{-1} h^{-1}	Solid-gas	water(10 μL)	42
UiO-66	CO 1.0 μmol g^{-1} h^{-1} CH_4 0.6 μmol g^{-1} h^{-1}	Solid-gas	water	43

Notes and references

[1] F. M. Zhang, L. Z. Dong, J. S. Qin, W. Guan, J. Liu, S. L. Li, M. Lu, Y. Q. Lan, Z. M. Su and H. C. Zhou, Effect of Imidazole Arrangements on Proton-Conductivity in Metal-Organic Frameworks, J. Am. Chem. Soc., 2017, **139,** 6183-6189.

[2] H. B. Luo, Q. Ren, P. Wang, J. Zhang, L. F. Wang and X. M. Ren, High Proton Conductivity Achieved by Encapsulation of Imidazole Molecules into Proton-Conducting MOF-808, ACS Appl. Mater. Interfaces., 2019, **11,** 9164-9171.

[3] P. G. M. Mileo, K. Adil, L. Davis, A. Cadiau, Y. Belmabkhout, H. Aggarwal, G. Maurin, M. Eddaoudi and S. Devautour-Vinot, Achieving Superprotonic Conduction with a 2D Fluorinated Metal-Organic Framework, J. Am. Chem. Soc., 2018, **140,** 13156-13160.

[4] S. Chand, W. H. Deng, A. Pal and M. C. Das, Polycarboxylate-Templated Coordination Polymers: Role of Templates for Superprotonic Conductivities of up to 10^{-1} S cm^{-1}, Angew. Chem. Int. Ed., 2018, **57,** 6662-6666.

[5] Y. X. Ye, W. G. Guo, L. H. Wang, Z. Y. Li, Z. J. Song, J. Chen, Z. J. Zhang, S. C. Xiang and B. L. Chen, Straightforward Loading of Imidazole Molecules into Metal-Organic Framework for High Proton Conduction, J. Am. Chem. Soc., 2017, **139,** 15604-15607.

[6] T. He, Y. Z. Zhang, H. Wu, X. J. Kong, X. M. Liu, L. H. Xie, Y. B. Dou and J. R. Li, Functionalized Base-Stable Metal-Organic Frameworks for Selective CO_2 Adsorption and Proton Conduction, ChemPhysChem., 2017, **18,** 3245-3252.

[7] J. Zhang, H. J. Bai, Q. Ren, H. B. Luo, X. M. Ren, Z. F. Tian and S. F. Lu, Extra Water- and Acid-Stable MOF-801 with High Proton Conductivity and Its Composite Membrane for Proton-Exchange Membrane, ACS Appl. Mater. Interfaces., 2018, **10,** 28656-28663.

[8] S. Khatua, A. K. Bar, J. A. Sheikh, A. Clearfield and S. Konar, Achieving Amphibious Superprotonic Conductivity in a CuI Metal-Organic Framework by Strategic Pyrazinium Salt Impregnation, Chem. Eur. J., 2018, **24,** 872-880.

[9] R. L. Liu, Y. R. Liu, S. H. Yu, C. L. Yang, Z. F. Li and G. Li, A Highly Proton-Conductive 3D Ionic Cadmium-Organic Framework for Ammonia and Amines Impedance Sensing, ACS Appl. Mat. Interfaces., 2019, **11,** 1713-1722.

[10] J. X. Wang, Y. D. Wang, M. J. Wei, H. Q. Tan, Y. H. Wang, H. Y. Zang and Y. G. Li, Inorganic open framework based on lanthanide ions and polyoxometalates with high proton conductivity, Inorg. Chem. Front., 2018, **5,** 1213-1217.

[11] P. Rought, C. Marsh, O. logo, S. Pili, V. G. Sakai, M. Li, M. S. Brown, S. P. Argent, I. Vitorica-Yrezabal, G. Whitehead, M. R. Warren, S. Yang and M. Schröder, Modulating proton diffusion and conductivity in metal-organic frameworks by incorporation of accessible free carboxylic acid groups, Chem. Sci., 2019,**10,** 1492-1499.

[12] S. S. Wang, X. Y. Wu, Z. Li, C. Z. Lu, Designed synthesis of a proton-conductive Ho-MOF

with reversible dehydration and hydration, Dalton Transactions., 2019, **48,** 9930-9934.
[13] G. Y. Zhang and H. H. Fei, Missing metal-linker connectivities in a 3-D robust sulfonate-based metal-organic framework for enhanced proton conductivity, Chem. Commun., 2017, **53,** 4156-4159.
[14] S. S. Park, A. J. Rieth, C. H. Hendon and M. Dincă, Selective Vapor Pressure Dependent Proton Transport in a Metal-Organic Framework with Two Distinct Hydrophilic Pores, J. Am. Chem. Soc., 2018, **140,** 2016-2019.
[15] H. B. Luo, Q. Ren, Y. Liu, Proton Conduction of an Acid-Resistant Open-Framework Chalcogenidometalate Hybrid in Anhydrous versus Humid Environments, Inorg. Chem., 2020, **59,** 7283-7289.
[16] R. L. Liu, W. T. Qu, B. H. Dou, Proton-Conductive 3D LnIII Metal-Organic Frameworks for Formic Acid Impedance Sensing, Chem Asian J., 2020, **15,** 182-190.
[17] K. Cai, F. Sun, X. Q. Liang, C. Liu, N. Zhao, X. Q. Zou and G. S. Zhu, An acid-stable hexaphosphate ester based metal-organic framework and its polymer composite as proton exchange membrane, J. Mater. Chem. A., 2017, **5,** 12943-12950.
[18] H. B. Luo, M. Wang, S. X. Liu, C. Xue, Z. F. Tian, Y. Zou and X. M. Ren, Proton Conductance of a Superior Water-Stable Metal-Organic Framework and Its Composite Membrane with Poly(vinylidene fluoride), Inorg. Chem., 2017, **56,** 4169-4175.
[19] H. Z. Sun, B. B. Tang and P. Y. Wu, Rational Design of S-UiO-66@GO Hybrid Nanosheets for Proton Exchange Membranes with Significantly Enhanced Transport Performance, ACS Appl. Mater. Interfaces., 2017, **9,** 26077-26087.
[20] B. Zhang, Y. Cao, Z. Li, H. Wu, Y. Yin, L. Cao, X. He, Z. Jiang, Responses to comments on "Ni nanoparticle-decorated reduced graphene oxide for non-enzymatic glucose sensing: An experimental and modeling study, Acta., 2017, **240,** 186-194.
[21] X. F. Zheng, X. Y. Zhao, J. Huang, H. Yang, Z. Liu, Photo-assisted green synthesis of silver doped silk fibroin/carboxymethyl cellulose nanocomposite hydrogels for biomedical applications, Appl Organomet Chem., 2020, e5981.
[22] F. L. Wang, C. Y. Liang, J. Y. Tang, F. Zhang, F. Y. Qu, The promotion of proton conductivity by immobilizing molybdovanadophosphoric acids in metal-organic frameworks, New J. Chem., 2020, **44,** 1912-1920.
[23] X. Meng, H. N. Wang, L. S. Wang, Y. H. Zou, Z. Y. Zhou, Enhanced proton conductivity of a MOF-808 framework through anchoring organic acids to the zirconium clusters by post-synthetic modification, CrystEngComm., 2019, **21,** 3146-3150.
[24] B. G. Montse, R. S. Ines, M. P. C. Rosario, Layered Lanthanide Sulfophosphonates and Their Proton Conduction Properties in Membrane Electrode Assemblies, Chem. Mater., 2019, **31,** 9625-9634.
[25] X. Gu, B. Li, F. L. Li, K. Zhang, M. H. Guo, Transparent and flexible vermiculite-cellulose nanofiber composite membranes with high-temperature proton conduction, J. Am. Chem. Soc., 2019, **54,** 5528-5535.
[26] M. Qiu, H. Wu, L. Cao, B. B. Shi, X. Y. He, H. B. Geng, X. L. Mao, P. F. Yang and Z. Y. Jiang. Metal-Organic Nanogel with Sulfonated Three-Dimensional Continuous Channels as a Proton Conductor, ACS Appl. Mater. Interfaces., 2020, **12,** 19788-19796.
[27] Q. Ren, J. W. Yu, H. B. Luo, J. Zhang, L. Wang, X. M. Ren, Design and Preparation of a

Superior Proton Conductor by Confining Tetraethylenepentamine in the Pores of ZIF-8 To Induce Further Adsorption of Water and Carbon Dioxide, Inorg. Chem., 2019, **58,** 14693-14700.
[28] L. Y. Wu, Y. F. Mu, X. X. Guo, Encapsulating Perovskite Quantum Dots in Iron-Based Metal-Organic Frameworks (MOFs) for Efficient Photocatalytic CO_2 Reduction, Angew. Chem. Int. Ed., 2019, **58,** 9491-9495.
[29] X. He, Z. R. Gan, S. Fisenko, D. W. Wang, H. M. El-Kader and W. N. Wang, Rapid Formation of Metal-Organic Frameworks (MOFs) Based Nanocomposites in Microdroplets and Their Applications for CO_2 Photoreduction, Acs Appl. Mater. Interfaces., 2017, **9,** 9688-9698.
[30] K. M. Choi, D. Kim, B. Rungtaweevoranit, C. A. Trickett, J. T. D. Barmanbek, A. S. Alshammari, P. D. Yang and O. M. Yaghi, Plasmon-Enhanced Photocatalytic CO_2 Conversion within Metal–Organic Frameworks under Visible Light, J. Am. Chem. Soc., 2017, **139,** 356-362.
[31] Q. Jiani, S. Wang, X. Wang, Visible-light reduction CO_2 with dodecahedral zeolitic imidazolate framework ZIF-67 as an efficient co-catalyst, Appl. Catal. B., 2017, **209,** 476-482.
[32] N. Li, J. Liu, J. J. Liu, L. Z. Dong, Z. F. Xin, Y. L. Teng, Y. Q. Lan, Adenine Components in Biomimetic Metal-Organic Frameworks for Efficient CO_2 Photoconversion, Angew. Chem. Int. Ed., 2019, **58,** 5226-5231.
[33] X. Y. Deng, Y. H. Qin, M. M. Hao and Z. H. Li, MOF-253-Supported Ru Complex for Photocatalytic CO_2 Reduction by Coupling with Semidehydrogenation of 1,2,3,4-Tetrahydroisoquinoline (THIQ), Inorg. Chem., 2019, **58,** 16574-16580.
[34] W. Y. Gao, H. T. Ngo, Z. Niu, W. J. Zhang, Y. X. Pan, Z. Y. Yang, V. R. Bhethanabotla, B. Joseph, Chemoenzymatic Synthesis of 5-Hydroxymethylfurfural (HMF)-Derived Plasticizers by Coupling HMF Reduction with Enzymatic Esterification, ChemSusChem., 2020, **13,** 1864-5631.
[35] Y. Tian, Y. Zhou, Y. Z. Zong, J. S. Li, N. Yang, M. Zhang, Z. Q. Guo and H. Song, Construction of Functionally Compartmental Inorganic Photocatalyst-Enzyme System via Imitating Chloroplast for Efficient Photoreduction of CO_2 to Formic Acid, ACS Appl. Mater. Interfaces., 2020, **12,** 34795-34805.
[36] X. S. Gao, B. Guo, C. M. Guo, Q. Meng, J. Liang and J. X. Liu, Zirconium-Based Metal-Organic Framework for Efficient Photocatalytic Reduction of CO_2 to CO: The Influence of Doped Metal Ions, ACS Appl. Mater. Interfaces., 2020, **12,** 24059-24065.
[37] J. Hu, J. Ding, Q. Zhong, In situ fabrication of amorphous TiO_2/NH_2-MIL-125(Ti) for enhanced photocatalytic CO_2 into CH_4 with H_2O under visible-light irradiation, J. Colloid. Interf. sci., 2020, **560,** 857-865.
[38] L. Wang, P. X. Jin, J. W. Huang, H. She and Q. Z. Wang, Integration of Copper(II)-Porphyrin Zirconium Metal-Organic Framework and Titanium Dioxide to Construct Z-Scheme System for Highly Improved Photocatalytic CO_2 Reduction, ACS Sustainable Chem. Eng., 2019, **7,** 15660-15670.
[39] Y. Xie, Z. B. Fang, L. Li, H. X. Yang and T. F. Liu, Creating Chemisorption Sites for Enhanced CO_2 Photoreduction Activity through Alkylamine Modification of MIL-101-Cr, ACS Appl. Mater. Interfaces., 2019, **11,** 27017-27023.
[40] L. Z. Dong, L. Zhang, J. Liu, Q. Huang, M. Lu, W. X. Ji and Y. Q. Lan, Stable Heterometallic Cluster-Based Organic Framework Catalysts for Artificial Photosynthesis, Angew. Chem. Int.

Ed., 2020, **59,** 2659-2663.

[41] S. Y. Chen, G. T. Hai, H. Y. Gao, X. Chen, A. Li, X. W. Zhang, W. J. Dong, Modulation of the charge transfer behavior of Ni(II)-doped NH_2-MIL-125(Ti): Regulation of Ni ions content and enhanced photocatalytic CO_2 reduction performance, Chem. Eng. J., 2021, **406,** 126886-126895.

[42] Z. C. Kong, J. F. Liao, Y. J. Dong, Y. F. Xu, H. Y. Chen, D. B. Kuang and C. Y. Su, Core@Shell $CsPbBr_3$@Zeolitic Imidazolate Framework Nanocomposite for Efficient Photocatalytic CO_2 Reduction, ACS Energy Lett., 2018, **3,** 2656-2662.

[43] Y. J. Ma, Q. Tang, W. Y. Sun, Z. Y. Yao, W. H. Zhu, T. Li, J. Y. Wang, Assembling ultrafine TiO_2 nanoparticles on UiO-66 octahedrons to promote selective photocatalytic conversion of CO_2 to CH_4 at a low concentration, Appl. Catal. B-Environ., 2020, **270,** 118856-118891.